Coherent Control of Bond Making

Liat Levin,[1] Wojciech Skomorowski,[2] Leonid Rybak,[1] Ronnie Kosloff,[3] Christiane P. Koch,[2] and Zohar Amitay[1]
[1]*The Shirlee Jacobs Femtosecond Laser Research Laboratory, Schulich Faculty of Chemistry, Technion-Israel Institute of Technology, Haifa 32000, Israel*
[2]*Theoretische Physik, Universität Kassel, Heinrich-Plett-Straße 40, 34132 Kassel, Germany*
[3]*Fritz Haber Research Centre and The Department of Physical Chemistry, Hebrew University, Jerusalem 91904, Israel*
(Received 5 November 2014; published 10 June 2015)

We demonstrate coherent control of bond making, a milestone on the way to coherent control of photoinduced bimolecular chemical reactions. In strong-field multiphoton femtosecond photoassociation experiments, we find the yield of detected magnesium dimer molecules to be enhanced for positively chirped pulses and suppressed for negatively chirped pulses. Our *ab initio* model shows that control is achieved by purification combined with chirp-dependent Raman transitions. Experimental closed-loop phase optimization using a learning algorithm yields an improved pulse that utilizes vibrational coherent dynamics in addition to chirp-dependent Raman transitions. Our results show that coherent control of binary photoreactions is feasible even under thermal conditions.

DOI: 10.1103/PhysRevLett.114.233003 PACS numbers: 42.65.Re, 82.50.Nd, 82.53.Eb, 82.53.Kp

A long-standing yet unrealized dream since the early days of coherent control, about 30 years ago, is the coherent control of photoinduced bimolecular chemical reactions [1,2]. Realizing this dream will create a new type of photochemistry with selective control of yields and branching ratios [3,4]. Shaped femtosecond laser pulses act there as special photocatalysts with a first pulse inducing and controlling the formation of a chemical bond, and a second time-delayed pulse breaking the desired bonds in the generated molecule. The second step, photodissociation into target channels with the desired branching ratios, has been demonstrated early on [5–11], once femtosecond lasers and pulse shaping technology became available. On the other hand, and in striking contrast, no experimental study has previously demonstrated coherent control of bond making. The photoinduced creation of a chemical bond between the colliding reactants, also termed photoassociation, using femtosecond laser pulses has proven to be much more challenging [12–16]. Particularly at high temperature, a typical situation for chemical reactions, the starting point for photoassociation is rather unfavorable to coherent control since many scattering states are incoherently populated. Unlike in the case of a bound initial state, a necessary requirement for the coherent control of photoassociation is thus preparation of quantum states with some purity and coherence. Key are vibrational coherences in the desired bond. As we have previously demonstrated with two-photon femtosecond photoassociation of hot magnesium atoms [16,17], such coherences can be generated by Franck-Condon filtering. This selects a subensemble out of the initial thermal ensemble, using the resonance condition for the laser excitation and exploiting correlations between rotational and translational motion [16]. These coherences should be amenable to coherent control.

Here we demonstrate coherent control of bond making in strong-field multiphoton femtosecond photoassociation (PA) of hot magnesium atoms. Our experimental results show the PA yield of detected Mg_2 molecules to be coherently controlled by linearly chirped pulses: The yield is strongly enhanced, compared to an unshaped transform-limited pulse, by positively chirping the pulses, and significantly suppressed for negatively chirped pulses. The measured PA yield is further enhanced by performing a closed-loop phase optimization of the best positively chirped pulse, using a genetic algorithm. Our *ab initio* model reveals the control mechanism to include purification via Franck-Condon filtering of collision energies and partial waves, chirp-dependent coherent Raman transitions, and vibrational coherent molecular dynamics. Our results prove that coherent control of binary photoreactions is feasible even under thermal conditions.

The bond-making excitation scheme for the free-to-bound PA process, $Mg + Mg + h\nu \rightarrow Mg_2^*$, is shown in Fig. 1(a): Pairs of magnesium atoms, part of an ensemble held at a temperature of 1000 K, collide in the $X\,^1\Sigma_g^+$ ground electronic state and are photoassociated via multiphoton transitions by an intense phase-shaped near-infrared (NIR) femtosecond pulse. The dominant process in the laser excitation is indeed bond formation [16,17]: The van der Waals well of the $X\,^1\Sigma_g^+$ state supports hardly any bound levels for partial waves with high J, which are preferentially populated at 1000 K. Thus about 80% of the UV signal originates from free-to-bound transitions [17]. The laser pulse is of linear polarization, 840 nm central wavelength, 13 nm bandwidth, and 70 fs transform-limited (TL) duration, with TL peak intensities of 5.0×10^{12} W/cm^2 or 7.2×10^{12} W/cm^2. At these intensities, bond-making transitions dominate over Mg_2 ionization,

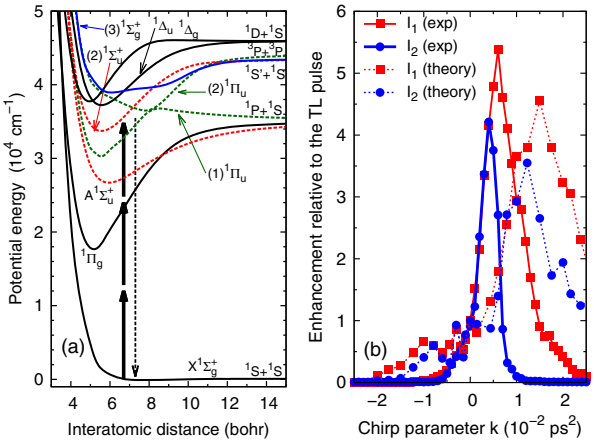

FIG. 1 (color online). (a) The bond-making photoassociation process involves excitation of pairs of atoms into bound levels of electronically excited states (bold arrows) which are monitored by UV emission (dotted arrow). (b) Emitted UV intensity as a function of the linear chirp parameter (squares are $I_{\mathrm{TL}} = 7.2 \times 10^{12}$ W/cm^2; circles are $I_{\mathrm{TL}} = 5 \times 10^{12}$ W/cm^2).

which requires at least five additional NIR photons. For the linearly chirped pulses, the spectral phase of the pulse is of the form $\Phi(\omega) = \frac{1}{2}k(\omega - \omega_0)^2$, with ω_0 the central frequency and k the linear chirp parameter. The PA process involves a broadband free-to-bound nonresonant two-photon transition from the $X\,^1\Sigma_g^+$ state to the excited $(1)\,^1\Pi_g$ state, as well as strong-field dynamics and resonant dipole transitions between the latter and higher-lying electronically excited states. The pulse shape controls the PA dynamics and the final populations of the various electronically excited states. Within this manifold, bound rovibrational levels of the $A\,^1\Sigma_u^+$, $(2)\,^1\Sigma_u^+$, and $(1)\,^1\Pi_u$ states emit UV light at 285.5–350.0 nm, below the $^1P \rightarrow {}^1S$ line of the Mg atom at 285.3 nm. The corresponding integrated UV intensity I_{UV} is proportional to the total population in these molecular states, reflecting the corresponding PA yield of Mg_2 molecules. This population is our control objective.

Experimentally, magnesium vapor of about 5 torr partial pressure in a heat pipe at 1000 K with Ar or He buffer gas is irradiated by shaped laser pulses. All our results are found to be independent of the choice of buffer gas. No magnesium clusters larger than dimers exist in the heat pipe [18]. The pulse shaping was done using a liquid-crystal spatial light phase modulator [19,20]. The UV radiation emitted toward the laser-beam entrance to the cell is collected at a small angle from the beam axis using a dichroic mirror, filter, and lens, focusing the UV light onto an optical fiber that is coupled to a spectrometer and a time-gated camera system with a 5-ns gate.

Coherent control of femtosecond photoassociation is demonstrated in Fig. 1(b) by plotting the UV signal I_{UV}, normalized with respect to the signal obtained for the TL pulse ($k = 0$), versus the chirp parameter k. An overall high degree of chirp control and a strongly asymmetric chirp dependence are observed. In particular, a large enhancement is obtained for positively chirped pulses whereas negatively chirped pulses lead to strong suppression. The chirp enhancement (E) also exhibits an intensity dependence, which is a clear indication of the strong-field regime: As the pulse energy, or, equivalently, the peak TL intensity I_{TL}, increases, the maximal enhancement $E_{\max}$ and the corresponding chirp $k_{\max}$ become larger. We find $E_{\max} = 4.2$ at $k_{\max} = 0.004$ ps^2 and $E_{\max} = 5.4$ at $k_{\max} = 0.006$ ps^2 for $I_{\mathrm{TL}} = 5.0 \times 10^{12}$ W/cm^2 and 7.2×10^{12} W/cm^2, respectively. The chirp enhancement rules out Mg ionization [21] to be responsible for the UV signal since such ionization should be most efficient here for TL pulses. This claim is further supported by the intensity dependence: The ratio between the UV signals measured with $I_{\mathrm{TL}} = 7.2 \times 10^{12}$ W/cm^2 and 5.0×10^{12} W/cm^2 is about 1.9. For NIR femtosecond ionization of magnesium atoms, the intensity dependence was found to scale as I^{11} for intensities up to 15×10^{12} W/cm^2 [21], corresponding to a signal ratio of about 55. Two linearly chirped pulses, one of positive chirp $|k|$ and the other of negative chirp $-|k|$, have identical instantaneous temporal intensity but different instantaneous temporal frequency and phase. Thus, the degree of coherent control is best reflected by the enhancement ratio $E(k_{\max})/E(-k_{\max})$. It amounts here to about 40 for $I_{\mathrm{TL}} = 7.2 \times 10^{12}$ W/cm^2, i.e., the experimentally observed PA yield is enhanced by this factor for the positively chirped pulse with $k = k_{\max} = 0.006$ ps^2 as compared to the negatively chirped pulse. This striking evidence of phase control calls for an explanation in terms of the underlying quantum molecular dynamics.

Our first-principles modeling utilizes the theoretical framework of Ref. [17], combining *ab initio* electronic structure theory with quantum dynamics in the presence of a strong laser field and thermal averaging based on random phase wave functions, neglecting couplings between rotations and vibrations. Here, we extend the model of Ref. [17] and explicitly account for all electronic states shown in Fig. 1(a), in order to improve the treatment of the Stark shifts for the electronically excited states [22]. The UV emission signal I_{UV} is calculated from the final populations of the $A\,^1\Sigma_u^+$, $(2)\,^1\Sigma_u^+$, and $(1)\,^1\Pi_u$ states via their Einstein coefficients. These states have a significant transition dipole moment to the $X\,^1\Sigma_g^+$ state and rovibrational levels that are located below the $^1P + {}^1S$ atomic threshold, giving rise to emission at wavelengths larger than 285.3 nm.

As Fig. 1(b) shows, our theoretical model clearly reproduces the main features of the experimental results—enhancement of the signal for positive chirp and suppression for negative chirp. The dependence on intensity, i.e., larger values of $E_{\max}$ and $k_{\max}$ for the larger intensity, is also predicted qualitatively correctly by the calculations. Quantitatively, the simulations show a slightly smaller peak enhancement, $E_{\max} = 4.5$ instead of 5.4 for the larger intensity; and the maximum is located at larger chirps

compared to the experimental data. The discrepancy with respect to $E_{\max}$ can easily be resolved by a small scaling of the $(1)\,^1\Pi_g$ Stark shift. For example, scaling this Stark shift by a factor of 0.95, well within the estimated error bounds of the calculated polarizabilities, increases $E_{\max}$ from 4.5 to 5.8. On the other hand, the shift in $k_{\max}$ is most likely linked to the relative slopes of the potentials of the $(1)\,^1\Pi_g$ state and all highly excited states that are accessed from it. Due to the number of electronic states that are involved, it is not possible to identify a single or few parameters whose change would result in an improved model. The inaccuracy of the highly excited states of Mg_2 in our model is confirmed by recent spectroscopy [23], which revealed the well depth of the adiabatic $(1)\,^1\Pi_u$ state to be larger by nearly 50% than the *ab initio* result [17]. This inaccuracy is not surprising: Potential energy curves of highly excited states are more prone to error since they often originate from the interaction between two open-shell excited-state atoms. This may lead to molecular electronic states that are very different from the reference ground state, requiring an even more correlated approach than the coupled cluster method with single and double excitations employed in Ref. [17]. Moreover, the high density of electronic states and the occurrence of possibly numerous avoided crossings between them result in a multireference nature of the electronic wave functions in the probed energy window which cannot be accurately described with a single-determinant assumption. More detailed spectroscopic data would be necessary to improve all relevant potential energy curves and allow for full quantitative agreement between theory and experiment.

The qualitative agreement observed in Fig. 1(b) is, however, certainly sufficient to examine the theoretical results in view of the mechanism that underlies the chirp control. To this end, Fig. 2(a) displays the chirp dependence of all population that is photoassociated, given by $1 - P_X$, with P_X the final population in the $X\,^1\Sigma_g^+$ ground electronic state, comparing it to the chirp dependence of the final population in the UV-emitting states: Whereas almost no chirp dependence is observed in the total PA yield $(1 - P_X)$, a clear chirp dependence is seen in the final populations of the emitting states, in particular a large asymmetry in the population of the $A\,^1\Sigma_u^+$ state. This suggests that the observed chirp dependence does not originate from the nonresonant $X\,^1\Sigma_g^+$ to $(1)\,^1\Pi_g$ transition, but results mainly from the strong-field dynamics on the $(1)\,^1\Pi_g$ and higher lying electronically excited states. If one assumes the last photon that excites into the UV-emitting states to constitute a weak probe, it is the shape of the vibrational distribution in the intermediate $(1)\,^1\Pi_g$ state that should be responsible for the chirp dependence of the signal in Fig. 1(b). Indeed, the final vibrational distribution in the $(1)\,^1\Pi_g$ state, plotted for various chirps in Fig. 2(b), shows a clear dependence on both sign and magnitude of the chirp parameter. This analysis is further supported by Fig. 2(c) which presents,

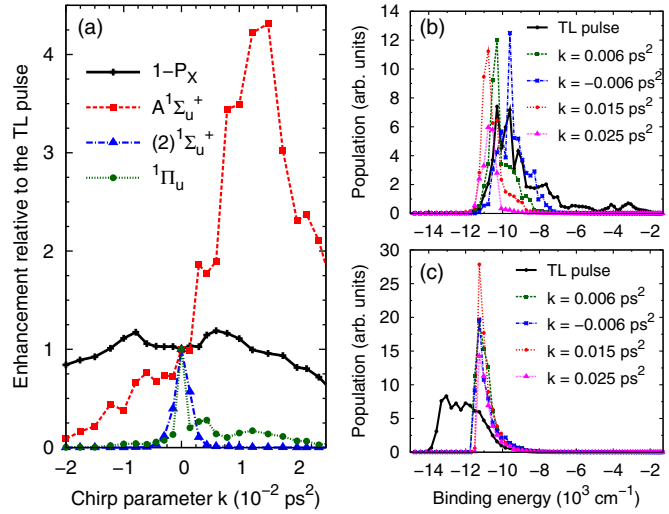

FIG. 2 (color online). Theoretical results ($I_{\mathrm{TL}} = 7.2 \times 10^{12}\,\mathrm{W/cm^2}$) for: (a) chirp dependence of the total photoassociated population $(1 - P_X)$ and the final populations in the states of the probed UV-emitting band. (b) Final vibrational distribution in the intermediate $(1)\,^1\Pi_g$ state for various values of the chirp parameter k. (c) Same as in (b) but obtained within a reduced model comprising only the $X\,^1\Sigma_g^+$ and $(1)\,^1\Pi_g$ states.

for comparison, the final vibrational distribution in the $(1)\,^1\Pi_g$ state, obtained within a reduced two-state model, comprising only the $X\,^1\Sigma_g^+$ and $(1)\,^1\Pi_g$ states. The results of the two-state model differ both qualitatively and quantitatively from those of the full model and show, in particular, no dependence on the sign of the chirp. The chirp dependence in the full model can then be rationalized in terms of resonant Raman transitions between the $(1)\,^1\Pi_g$ state and the higher-lying u states: The instantaneous frequency of the chirped pulse leads to an up (down) shift of the $(1)\,^1\Pi_g$ vibrational distribution for negative (positive) chirp. The magnitude of the up- or down-shift depends on the absolute value of the chirp parameter. Down-shifting the $(1)\,^1\Pi_g$ vibrational distribution results in an enhanced UV emission signal because it favors transitions into bound levels of the $A\,^1\Sigma_u^+$ state in the probed UV-emitting band, whereas an up-shifted $(1)\,^1\Pi_g$ vibrational distribution is predominantly excited into dissociative states which do not contribute to the molecular emission signal. Our picture of a perturbative final probe photon is confirmed by comparing the calculated final vibrational distributions in the UV emitting states to the Franck-Condon projection of the final $(1)\,^1\Pi_g$ distribution onto these states. The narrowing of the vibrational distribution due to the chirp, observed in both Figs. 2(b) and 2(c), is readily understood in terms of a competition between nonresonant Stark shifts and chirp. The chirp lowers the peak intensity and thus the Stark shift such that less power broadening of the vibrational distribution is induced by the chirped pulses as compared to the TL pulse.

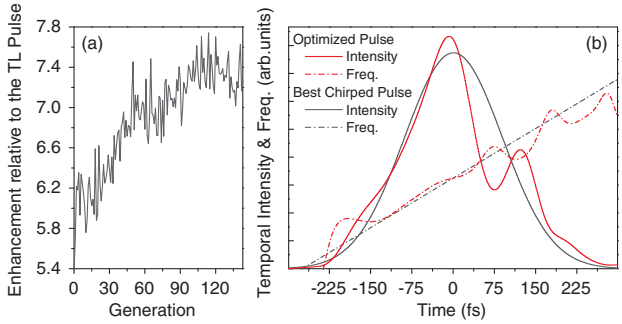

FIG. 3 (color online). Results for experimental closed-loop phase optimization using a learning algorithm, starting from the best linearly chirped pulse. (a) Enhancement as a function of generation; improvement is very fast. (b) The optimized pulse compared to the best linearly chirped pulse ($k = 0.006$ ps^2).

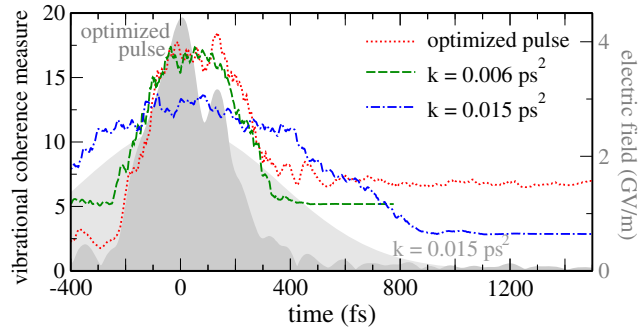

FIG. 4 (color online). Role of vibrational coherence in the $(1)\,^1\Pi_g$ state (with the optimized and linearly chirped pulses in grey).

Figure 2(b) also indicates why a chirp rate of $k = 0.015$ ps^2 is optimal: For even larger chirps, we do not observe a further down-shift of the $(1)\,^1\Pi_g$ vibrational distribution. This is attributed to both the limited bandwidth of the pulse and the significantly reduced peak intensity for larger chirps. Thus, the optimal chirp results from a competition between sufficient intensity for the Raman transitions and down-shifting of the vibrational distribution. This interpretation is also supported by the larger peak enhancement observed for the larger intensity in Fig. 1(b).

Our understanding of the control being facilitated by shaping the vibrational $(1)\,^1\Pi_g$ distribution suggests further enhancement of the PA signal to be possible by exploiting the $(1)\,^1\Pi_g$ vibrational dynamics, in addition to the Raman transitions. To explore this possibility, we have experimentally carried out an automated closed-loop phase optimization using a learning algorithm [6], with the enhancement relative to the TL pulse as performance criterion. Every generation of the learning algorithm contains 24 members, i.e., spectral phase patterns applied to the pulse. The first generation includes the five best linearly chirped pulses, with $k = 0.004$ ps^2 to 0.008 ps^2, while all other members are random. Figure 3(a) shows the maximally obtained PA enhancement as a function of the generation number. A fast increase of about 35% in the maximum enhancement is observed, from a value of 5.4 for $k_{\max} = 0.006$ ps^2 to a value of about 7.4 after 130 generations. The two corresponding pulses, i.e., the best linearly chirped pulse and the optimized pulse, are shown in Fig. 3(b). The optimization keeps the positive linear chirp, and additionally splits the pulse into two subpulses with a time delay of 130 fs. This delay corresponds to the vibrational period of the $(1)\,^1\Pi_g$ levels in the excitation region. It indicates that the optimized pulse utilizes the vibrational dynamics for improving the PA enhancement.

When testing the experimentally optimized pulse in our theoretical model, the enhancement is increased by 60% for $k = 0.006$ ps^2. Compared to the best linearly chirped pulse ($k_{\text{theor}} = 0.015$ ps), the optimized pulse is found to populate a significantly broader vibrational band in the $(1)\,^1\Pi_g$ state, with more population in the lower levels with one-photon transitions into the probed UV-emitting band. The role of coherent vibrational dynamics in the $(1)\,^1\Pi_g$ state is further analyzed in Fig. 4 which displays the vibrational coherence measure [24], $\mathcal{C}(t) = \sum_{i\neq j}|\rho_{ij}^{\Pi_g}(t)|$ of the normalized $(1)\,^1\Pi_g$ density [25]. The values of $\mathcal{C}(t)$ in Fig. 4 need to be compared to the upper bound of the maximally coherent state, $d - 1$, where d is the number of levels, about 70 in our case. We thus find a substantial amount of vibrational coherence in the $(1)\,^1\Pi_g$ state. In particular at intermediate times, when the dynamics in the $(1)\,^1\Pi_g$ state is relevant, the coherence measure is larger for the optimized pulse than for the chirped pulses. The optimized pulse thus outperforms the chirped pulses by utilizing coherent vibrational dynamics in the $(1)\,^1\Pi_g$ state, in addition to the chirp-dependent Raman transitions.

In summary, we observe strong-field coherent control of bond formation in the femtosecond photoassociation of hot magnesium atoms using phase-shaped laser pulses. Our modeling from first principles has allowed us to identify a combination of Franck-Condon filtering in the free-to-bound nonresonant two-photon step with chirp-dependent resonant Raman transitions and coherent vibrational dynamics in an intermediate electronic state to be responsible for the control. Whereas the purpose of the Franck-Condon filtering is mainly purification in order to allow the generation of molecular coherence, the Raman transitions and vibrational dynamics serve to realize phase control. Indeed, the quantum purity in the intermediate state and final UV-emitting states differ by only 25% for the experimentally optimal linear chirp. Our demonstration of coherent control of bond-making under thermal conditions points the way toward controlling transition probabilities and branching ratios to different target states. For photoinduced chemical reactions with several product channels, suitable target states would be those that serve as a gateway to a different product channel. A feasible route to the coherent control of photoinduced bimolecular chemical reactions is now open.

We would like to thank Daniel Reich for technical help at an initial stage of this work. This research was supported by The Israel Science Foundation (Grant No. 1450/10) and the Alexander von Humboldt Foundation (W. S.).

L. L. and W. S. contributed equally to this work.

[1] D. Tannor and S. A. Rice, J. Chem. Phys. **83**, 5013 (1985).
[2] R. Kosloff, S. Rice, P. Gaspard, S. Tersigni, and D. Tannor, Chem. Phys. **139**, 201 (1989).
[3] S. A. Rice and M. Zhao, *Optical Control of Molecular Dynamics* (John Wiley & Sons, New York, 2000).
[4] P. Brumer and M. Shapiro, *Principles and Applications of the Quantum Control of Molecular Processes* (Wiley Interscience, New York, 2003).
[5] R. J. Gordon and S. A. Rice, Annu. Rev. Phys. Chem. **48**, 601 (1997).
[6] T. Brixner and G. Gerber, ChemPhysChem **4**, 418 (2003).
[7] M. Dantus and V. V. Lozovoy, Chem. Rev. **104**, 1813 (2004).
[8] M. Wollenhaupt, V. Engel, and T. Baumert, Annu. Rev. Phys. Chem. **56**, 25 (2005).
[9] O. Kühn and L. Wöste, eds., *Analysis and Control of Ultrafast Photoinduced Reactions* (Springer, Berlin, 2007).
[10] R. J. Levis, G. M. Menkir, and H. Rabitz, Science **292**, 709 (2001).
[11] H. Rabitz, R. de Vivie-Riedle, M. Motzkus, and K. Kompa, Science **288**, 824 (2000).
[12] U. Marvet and M. Dantus, Chem. Phys. Lett. **245**, 393 (1995).
[13] W. Salzmann, T. Mullins, J. Eng, M. Albert, R. Wester, M. Weidemüller, A. Merli, S. M. Weber, F. Sauer, M. Plewicki *et al.*, Phys. Rev. Lett. **100**, 233003 (2008).
[14] P. Nuernberger, D. Wolpert, H. Weiss, and G. Gerber, Proc. Natl. Acad. Sci. U.S.A. **107**, 10366 (2010).
[15] L. Rybak, Z. Amitay, S. Amaran, R. Kosloff, M. Tomza, R. Moszynski, and C. P. Koch, Faraday Discuss. Chem. Soc. **153**, 383 (2011).
[16] L. Rybak, S. Amaran, L. Levin, M. Tomza, R. Moszynski, R. Kosloff, C. P. Koch, and Z. Amitay, Phys. Rev. Lett. **107**, 273001 (2011).
[17] S. Amaran *et al.*, J. Chem. Phys. **139**, 164124 (2013).
[18] P. J. Ziemann and A. W. Castleman Jr., Z. Phys. D **20**, 97 (1991).
[19] A. M. Weiner, Rev. Sci. Instrum. **71**, 1929 (2000).
[20] T. Brixner and G. Gerber, Opt. Lett. **26**, 557 (2001).
[21] G. D. Gillen, M. A. Walker, and L. D. Van Woerkom, Phys. Rev. A **64**, 043413 (2001).
[22] In detail, the Hamiltonian in Eq. (12) of Ref. [17] has been augmented to include four additional states, $(1)\,^1\Delta_g$ (dissociating into $^1D + {}^1S$ atoms), $(1)\,^1\Delta_u$ $(^1D + {}^1S)$, $(2)\,^1\Sigma_g^+$ $(^1S + {}^1S^\star)$, and $(3)\,^1\Sigma_u^+$ $(^3P + {}^3P)$. If not accounted for explicitly, these states cause resonances in the Stark shifts of the lower-lying states.
[23] H. Knöckel, S. Rühmann, and E. Tiemann, Eur. Phys. J. D **68**, 293 (2014).
[24] T. Baumgratz, M. Cramer, and M. B. Plenio, Phys. Rev. Lett. **113**, 140401 (2014).
[25] $C(t)$ counts the off-diagonal matrix elements of the density matrix, i.e., the coherences. Following Ref. [17], the total density matrix is obtained as an incoherent sum over each propagated random phase wave function, $\rho(t) = (1/ZN)\sum_{k=1}^{N}\sum_{J=0}^{J_{\max}}(2J+1)|\Psi_J^k(t)\rangle\langle\Psi_J^k(t)|$, where Z denotes the partition function and k runs over random phase realizations. $\rho_{ij}^{\Pi_g}(t)$ is obtained analogously, using the $(1)^1\Pi_g$ component of $|\Psi_J^k(t)\rangle$. Since we neglect rotational coherences, only vibrational coherences are accounted for.